Advanced passivity-based, aging-tolerant control for a fuel cell/super-capacitor hybrid system

Suyao Kong, Mathieu Bressel, Mickaël Hilairet, Robin Roche

Advanced Passivity-Based, Aging-Tolerant Control for a Fuel Cell/Super-Capacitor Hybrid System

S. Kong[a,b], M. Bressel[c], M. Hilairet[a,b], R. Roche[a,b]

[a] *FEMTO-ST Institute, Univ. Bourgogne Franche-Comté, UTBM, CNRS*
Rue Ernest Thierry Mieg, F-90000 Belfort, France
[b] *FCLAB, Univ. Bourgogne Franche-Comté, UTBM, CNRS*
Rue Ernest Thierry Mieg, F-90010 Belfort, France
[c] *CRIStAL, CNRS 9189, Ecole des Hautes Etudes d'Ingénieur (HEI),*
13 rue de Toul, F-59046 Lille, France
e-mail: mickael.hilairet@univ-fcomte.fr

Abstract

This paper proposes an advanced aging-tolerant control for a fuel cell/super-capacitor hybrid system applied to a commercial vehicle. The controller is designed with the Interconnection and Damping Assignment - Passivity-Based Control (IDA-PBC) method to solve the converters coordination problem, where the state-of-charge of the super-capacitors and all current limitations are considered into the non-linear controller. The aging of the fuel cell is estimated in real-time by an extended Kalman filter and is integrated in the controller in order to preserve the stability of the whole system. Finally, a hardware-in-the-loop platform based on an INTEL/ALTERA FPGA is designed in order to validate the real-time operation of the algorithms for a specific case study with a fuel cell vehicle.

Keywords: Fuel cell, super-capacitors, power management, port-controlled Hamiltonian systems, Interconnection and Damping Assignment - Passivity-Based Control (IDA-PBC), Hardware-in-the-loop platform, INTEL/ALTERA FPGA.

1. Introduction

Using hydrogen and fuel cells (FCs) is a promising way to deal with environmental problems and fossil fuels shortage. As electric and hybrid vehicles are becoming more and more popular, fuel cell vehicles (FCVs) are also considered due to their fast recharge time, low weight and controllability. For several decades, FCVs have been developed with the goal of decreasing air pollution, oil dependence as well as greenhouse gases emissions. However, high costs, limited durability and reliability are among the aspects that need to be improved for such vehicles.

Among the various types of FC systems, Proton Exchange Membrane Fuel Cell (PEMFCs) have been found to be especially suitable for hybrid energy systems because of their high power density and low operating temperature. However, PEMFC systems have a limited lifetime because of multiple impairments that prevent their widespread deployment.

As a consequence, prognostics and health management (PHM) of PEMFCs is mandatory for industrial applications. PHM allows extending the life of such electrochemical converters using monitoring [1], diagnostics [2], [3], prognostics [4], and corrective actions. The indicators of the state-of-health (SoH) of an FC system can be built by selecting specific features from sensors [5]. This allows the planning of preventive maintenance at the right time, resulting in reduced costs. In the field of energy management, knowing the SoH and remaining life of an energy source (e.g., batteries and PEMFCs) can help improve the power and energy distribution among the different components in the system.

In order to maximise their useful life, FCs must have slow power dynamics and a hybrid source system is, therefore, necessary for FCVs. Usually, in a FC hybrid system, the FC is the main power source and batteries (BTs) or super-capacitors (SCs) are transient power sources. A FC is also usually associated with SCs for their high dynamics, as batteries sometimes cannot sustain very high power charge and discharge conditions. SCs are often considered as the best choice for fast power demands due to their ability to operate well at low temperatures, and are industrially manufactured.

Many research studies on FC/SCs or BTs/SCs hybrid systems have been published [6, 7, 8, 9, 10] . One more element is sometimes added, such as a battery [11, 12, 13, 14, 15, 16] or a wind turbine [17, 18] for microgrid applications [19]. Fuzzy logic, passivity-based control [6, 20, 21, 22], flatness based control [23], Lure-Lyapunov theory [24], Lyapunov-based nonlinear control [25, 26], adaptive second order sliding mode control [27], adaptive control [28], Model Predictive Control (MPC) [13], regular controllers or optimization algorithms [29] are typically used in the controller design of such systems. These controllers are based on the same principle, i.e. to decide the power and energy sharing between the sources. However, a perfect coordination of the sources is rarely studied in normal conditions [30], and even more during abnormal working conditions, such as with power limitations due to aging phenomena or current limitations of the FC or SCs with rigorous stability analysis of the closed-loop system under all constraint situations.

In this paper, an energy management strategy is first realized by the Interconnection and Damping Assignment - Passivity-Based Control (IDA-PBC) method, based on a significant extension of previous work [31, 32]. The new IDA-PBC controller integrates components constraints and shows that: i) The SCs reference current can be a function of the SCs voltage. Here, a good choice of a tuning parameter (r_2) allows modifying the SCs reference current according to the state of the SCs. ii) When the SCs voltage is low or too high, parameter r_2 is different from zero and impacts the FC current. Therefore, the FC can compensate for the power that the SCs cannot provide. iii) A controlled charge is activated in order to dissipate the extra power during a regenerative mode when the SCs voltage is too high.

Firstly, all these new ideas are introduced in the proposed controller based on passivity. The energy management system guarantees that all the power sources respect the components constraints and the closed-loop stability is analysis for all the mode of operation. Secondly, an Extended Kalman Filter (EKF) based on [33, 34] provides the actual and forecast SoH of the FC in real-time in order to compute the maximum current and power that the FC can deliver. Based on such information, it is guaranteed that the closed-loop power management system cannot diverge.

This paper is divided into four sections: Section 2 describes the hybrid model of a specific case study and the aging of the FC. The proposed passivity-based controller is detailed in sections 3 and 4. In section 5, a ageing-tolerant controller is described and results are provided in section 6 based on a Hardware-In-the-Loop (HIL) platform representative of a commercial vehicle under a NEDC driving cycle.

2. Hybrid System Modeling and Control Structure

2.1. Aging Model of the PEMFC

In this research, a static model of FC is employed. It is described with the following equation [33, 34]:

$$v_{fc} = n\left(E_0 - AT_{fc}\ln\left(\frac{j_{fc}}{j_0}\right) - Rj_{fc} - BT_{fc}\ln\left(1-\frac{j_{fc}}{j_L}\right)\right) \tag{1}$$

where $j_{fc} = \frac{i_{fc}}{S}$ is the input current density, i_{fc} the FC current and S the activation surface of the FC. This relation is used to model the polarization curve $v_{fc} = f(i_{fc})$, where v_{fc} is the FC voltage, n the number of cells, E_0 represents the maximum theoretical potential, T_{fc} is the operation temperature, A and B represent the activation and concentration constants, R is the

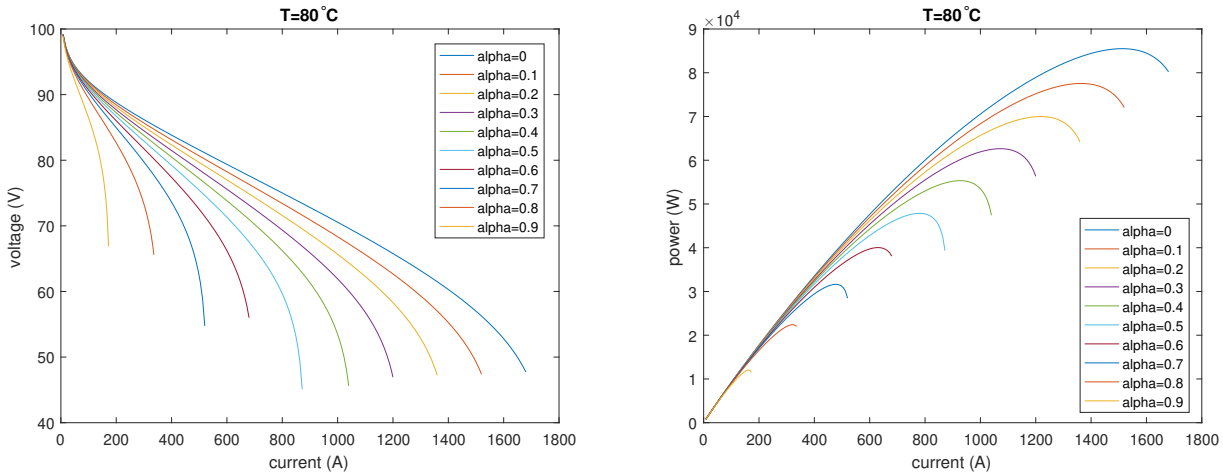

Figure 1: V-I and P-I curves of the FC at $80°C$

global resistance related to membranes, electrodes and connectors, j_0 is the exchange current density and j_L is the limiting current density. All parameter values are listed in Table 1.

In order to study the effect of aging on the parameter values of (1), a 175-hour continuous experimental test was performed on an 8-cell FC stack under an automotive load profile with a surface of $220\,\mathrm{cm}^2$, provided by the French Atomic Energy and Alternative Energies Commission (CEA) (see [35] for more details about the FC operating conditions). Using a fitting technique, a set of model parameters were extracted from these curves [33]. It was observed that only the resistance value R and the limiting current density j_L change significantly. Based on the above studies, an empirical degradation model has been developed and is described as follows:

$$R(t) = R_0(1 + \alpha(t)),\ j_L(t) = j_{L0}(1 - \alpha(t)) \tag{2}$$

$$\alpha(t) = \int_0^t \beta(\tau)d\tau \tag{3}$$

where $\alpha(t)$ is the SoH indicator, $\beta(t)$ is the rate of change of the parameter $\alpha(t)$, i.e. $\beta(t) = d\alpha(t)/dt$, and R_0 and j_{L0} are the initial resistance and limiting current density extracted from the first polarization curve. Note that $\alpha(t)$ and $\beta(t)$ are unknow time varying parameters and that is the role of an observer to estimate its in real-time (see section 5). SoH $\alpha(t)$ is set equal to zero at the beginning (i.e., no degradation), and increases to $\alpha_{max} = 0.3$ at the considered End-of-Life (EoL) of the FC. A value of α_{max} equal to 0.3 represents a reduction of around 10% of the nominal power of the FC at $0.5\,\mathrm{A/cm}^2$ (see [33, 34, 35] for more details).

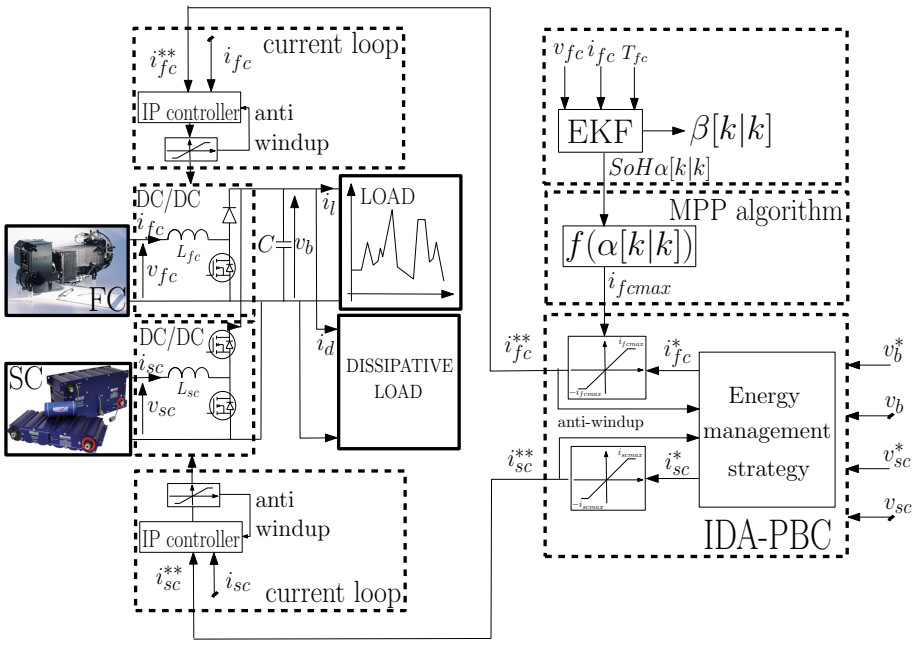

Figure 2: Two-converter structure and control architecture

Fig. 1 shows the polarization curve and power at 80°C for the considered application example with different SoH levels, where the number of cells of one FC module has been fixed at 53. For the purpose of the case study, two FC modules in series and eight in parallel were connected in order to obtain a total power of 85 kW for a healthy new FC. **Based on the right plot of Fig. 1, it is apparent that the controller needs to know the maximum current that the FC can deliver over time. Without that knowledge, the whole hybrid closed-loop system diverges, leading to an unstable system** because of FC reference current runaway. In fact, due the FC power characteristic (see Fig. 1), if the FC reference current becomes greater than the maximum FC current, the power delivered by the FC decreases leading to an increase of the FC reference current. The maximum current of the FC over time is obtained in two steps. First, the SoH is estimated by an EKF. Second, the maximum power point (MPP) of the FC can be determined from the P-I curve of the FC. The limitation of the FC reference current is set to 80% of the MPP and sent to the power management controller in order to protect the FC from overload.

2.2. Hybrid System Modeling

A two-converter parallel structure of a FC/SCs system is applied in this work, as shown in Fig. 2, where the architecture of the power management control as well as the aging-tolerant control

and the architecture of the power converters are represented.

In this system, SCs are connected to the DC bus through a reversible boost converter. The load is modeled by a variable current source in order to model generative and motor conditions. Moreover, an additional dissipative charge is added and activated in the case of limitation of the SCs during a generative mode of the load. Without this protection, the DC bus voltage can rise significantly and the dissipative charge is used to prevent such circumstances, such as in railway or automotive applications.

The complete system is represented by the following 4^{th} order non-linear state space model:

$$\begin{array}{rcl} \frac{d}{dt}v_b(t) & = & \frac{(1-\alpha_1(t))\,i_{fc}(t)+(1-\alpha_2(t))\,i_{sc}(t)-i_l(t)-i_d^*(t)}{C} \\ \frac{d}{dt}v_{sc}(t) & = & -\frac{i_{sc}(t)}{C_{sc}} \\ \frac{d}{dt}i_{fc}(t) & = & \frac{-(1-\alpha_1(t))\,v_b(t)+v_{fc}(t)}{L_{fc}} \\ \frac{d}{dt}i_{sc}(t) & = & \frac{-(1-\alpha_2(t))\,v_b(t)+v_{sc}(t)}{L_{sc}} \end{array} \tag{4}$$

with state $[v_b(t),\, v_{sc}(t),\, i_{fc}(t),\, i_{sc}(t)]^T$, the duty cycles as control inputs $[\alpha_1(t), \alpha_2(t)]^T$, and measurements $v_b(t), v_{sc}(t), v_{fc}(t), i_{fc}(t), i_{sc}(t), i_l(t)$ and $i_d(t)$. Variable $\alpha_{1,2}(t)$ represents the duty cycle of the converters, $v_b(t)$ is the DC bus voltage, $v_{fc}(t)$, $v_{sc}(t)$ are the FC and SCs voltage, $i_{fc}(t)$, $i_{sc}(t)$ are the FC and SCs current, $i_l(t)$ is the DC current consumed by the load, and $i_d^*(t)$ a controllable current source that represents the current consumed by the dissipative resistance load to protect the system. The definitions and values of the parameters are given in Table 1.

Because of the difference of time scale between the voltages and the currents, the system is called a singular perturbed system (see appendix B.3 of [36]). In fact, parameters L_{fc} and L_{sc} are small compared to parameters C and C_{sc} [20], therefore, the 4^{th} order non-linear state space model can be reduced to a 2^{nd} order system to design the outer loop controller as follows:

$$\begin{array}{rcl} \frac{d}{dt}v_b(t) & = & \frac{1}{C}\left(\frac{v_{fc}(t)}{v_b(t)}\,i_{fc}^*(t) + \frac{v_{sc}(t)}{v_b(t)}\,i_{sc}^*(t) - i_l(t) - i_d^*(t)\right) \\ \frac{d}{dt}v_{sc}(t) & = & -\frac{i_{sc}^*(t)}{C_{sc}} \end{array} \tag{5}$$

with $x_r(t) = [x_1,\, x_2]^T = [v_b,\, v_{sc}]^T$, control inputs $u_r = [i_{fc}^*,\, i_{sc}^*]^T$, and measurements $y_r = [v_b,\, v_{sc}]^T$.

In order to protect the equipment, controlling the current is mandatory for industrial applications. Therefore, the control is composed of two parts: two fast inner current control loops and two slower outer voltage loops, where the first controllers are based on Integral-Proportional IP

controllers associated with anti-windup [37] (see Table 1 for the gain values), and the DC bus voltage and state-of-charge of the SCs are controlled by IDA-PBC.

2.3. Vehicle modeling and load current computation

A case study based on a commercial vehicle, a Renault Master [10], is considered in this work. The load current $i_l(t)$ is calculated by:

$$i_l(t) = \frac{P_{vehicle}(t)}{v_b(t)} \tag{6}$$

where the electrical power $P_{vehicle}$ demanded by the vehicle is

$$P_{vehicle} = F_{traction} V_{vehicle} (\eta_{traction})^k \tag{7}$$

with $k = 1$ if $P_{vehicle} < 0$ and $k = -1$ if $P_{vehicle} > 0$. $F_{traction}$ is the traction force, $V_{vehicle}$ is the vehicle velocity and $\eta_{traction}$ is the transmission efficiency. Next, according to Newton's second law of motion, we have:

$$M_{tot} \frac{d}{dt} V_{vehicle} = F_{traction} - F_{res} \tag{8}$$

where the total amount of resistant forces F_{res} is represented by a quadratic function of the vehicle speed [10]:

$$F_{res} = F_0 + F_a V_{vehicle}^2 \tag{9}$$

Here, F_0 is the road slope and rolling resistant force and F_a is the aerodynamic drag resistance, which can be calculated by [38, 39]:

$$F_0 = mgf_r \tag{10}$$

$$f_r = 0.01 \left(1 + \frac{V_{vehicle}}{100}\right) \tag{11}$$

$$F_a = \frac{1}{2} \rho C_x S_{vehicle} \tag{12}$$

where $S_{vehicle}$ is the vehicle front area, ρ is the air density, and C_x is the vehicle aerodynamic drag coefficient.

3. Controller Design Using IDA-PBC

Rewriting the open-loop function (5), the plant can be defined as:

$$\dot{x}_r = f(x_r) + g(x_r) u_r + d \tag{13}$$

with

$$x_r = [v_b,\, v_{sc}]^T \tag{14}$$

$$u_r = [i^*_{fc},\, i^*_{sc}] \tag{15}$$

$$f(.) = \begin{bmatrix} 0 & 0 \\ 0 & 0 \end{bmatrix} \tag{16}$$

$$g(.) = \begin{bmatrix} \frac{1}{C}\frac{v_{fc}}{v_b} & \frac{1}{C}\frac{v_{sc}}{v_b} \\ 0 & -\frac{1}{C_{sc}} \end{bmatrix} \tag{17}$$

$$d(.) = \begin{bmatrix} -i_l - i^*_d \\ 0 \end{bmatrix} \tag{18}$$

where time dependence has been omitted for simplicity.

Assume that there are matrices $\mathcal{J}_d(.) = -\mathcal{J}_d^t(.)$, $\mathcal{R}_d(.) = \mathcal{R}_d^t(.) \geq 0$ and $g^\perp(.)$ a full-rank annihilator of $g(.)$, i.e. $g^\perp g = 0$ and a function $\mathcal{H}_d : \Re^n \longrightarrow \Re$ that verify the partial differential equation (PDE)

$$g^\perp(x_r) f(x_r) = g^\perp(x_r)[\mathcal{J}_d(x_r) - \mathcal{R}_d(x_r)]\nabla\mathcal{H}_d \tag{19}$$

The closed-loop system (13) takes the desired Port-Controlled Hamitonian (PCH) form

$$\dot{x}_r = [\mathcal{J}_d(x_r) - \mathcal{R}_d(x_r)]\nabla\mathcal{H}_d \tag{20}$$

with the control law u_r as

$$u_r = \left[g^T(x_r)g(x_r)\right]^{-1} g^T(x_r)\left\{[\mathcal{J}_d(x_r) - \mathcal{R}_d(x_r)]\,\nabla\mathcal{H}_d - f(x_r) - d\right\} \tag{21}$$

where the desired Hamiltonian function $\mathcal{H}_d$ is first selected (a quadratic function in the error terms, i.e. $\mathcal{H}_d = \frac{1}{2}(C\tilde{v}_b^2 + C_{sc}\tilde{v}_{sc}^2)$) and $\mathcal{J}_d(.)$ and $\mathcal{R}_d(.)$ are free tuning matrices of the closed-loop dynamics. This IDA-PBC procedure refers to the algebraic IDA-PBC technique in order to avoid the difficult resolution of PDE (19) of the non-parameterized IDA-PBC technique (see [40] for more details). The application of LaSalle's theorem to $\mathcal{H}_d$ [41] proves the asymptotic stability of the closed-loop system [40, 42]. The development of (21) leads to the following non-linear control law:

$$\delta\dot{y} = -y + i_l/v_b, \qquad \delta > 0 \tag{22}$$

$$i^*_{fc} = \frac{v_b}{v_{fc}}\left(y v_b^* - \gamma\tilde{v}_{sc} - r_2\frac{v_{sc}}{v_b}C_{sc}^2\tilde{v}_{sc} + i^*_d + (\frac{v_{sc}}{v_b}\gamma - r_1C^2)\tilde{v}_b\right), \qquad \gamma > 0 \tag{23}$$

$$i^*_{sc} = -\gamma\,\tilde{v}_b + r_2C_{sc}^2\tilde{v}_{sc} \tag{24}$$

with

$$\mathcal{J}_d = \begin{bmatrix} 0 & J_{12} \\ -J_{12} & 0 \end{bmatrix}, \quad \mathcal{R}_d = \begin{bmatrix} r_1 & 0 \\ 0 & r_2 \end{bmatrix}, \quad \nabla\mathcal{H}_d = \begin{bmatrix} C\,\tilde{v}_b \\ C_{sc}\,\tilde{v}_{sc} \end{bmatrix}$$

where J_{12} is set equal to $-\frac{\gamma}{CC_{sc}}$, $\gamma > 0$ (to simplify notations) and the current load i_l is filtered by an estimation of admittance y [31]. Parameters γ and δ are positive tuning parameters of the controller and the admittance estimator, respectively (see Table 1).

4. Advanced Power Management Strategy

4.1. Objective

The objective of the new controller is to define appropriate values of parameters r_1 and r_2 with the equation used to calculate the controllable dissipative load i_d^* (see (23)) in order to preserve the stability of the whole closed-loop system while ensuring the limiting constraints of the components. Compared to the proposition in [31] (see also [31] for a comparison with regular PI controllers) r_2 is possibly different from zero thus integrating the state-of-charge of the SCs directly in the controller (see (24)).

4.2. Normal Operation

During normal operation of the FC and SCs, i.e., with less than the maximum values of currents and voltages, the dissipative load current i_d^* is equal to zero. In order to increase the lifetime of the FC, it does not seem sensible that the FC current participates in the control of the DC bus voltage, nor that we dissipate energy in the controllable load. Therefore, the term $\left(\frac{v_{sc}}{v_b}\gamma - r_1 C^2\right)\tilde{v}_b$ in (23) is set to zero, which leads to r_1 equal to $\frac{v_{sc}\gamma}{v_b C^2}$. As for the control method proposed in [43], the DC bus voltage is managed only by the SCs, so r_2 is set equal to zero (see (24)).

4.3. SCs Voltage Limitation

In practice, the SCs voltage usually fluctuates within range $[v_{scL}, v_{scH}]$. If the SCs voltage exceeds these limits, constraints are added to limit the charge or discharge of the SCs depending on the mode of operation. Fig. 3.a shows a specific saturation function that represents these limitations [43].

This saturation is integrated directly into the controller to preserve the stability property of the passivity controller as follows:

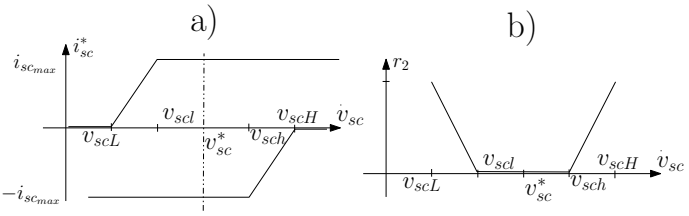

Figure 3: Saturation functions of the reference current i^*_{sc} and evolution of r_2 according to the SCs voltage.

- When the SCs voltage is low ($v_{scL} < v_{sc} < v_{scl}$), the discharge of the SCs is limited during a discharge operation. $r_2 > 0$ then has a linear relationship with $\tilde{v}_{sc}$. From this, we also benefit from an acceleration of the SCs charge when the system is operating in generation mode.

- When the SCs voltage is high ($v_{sch} < v_{sc} < v_{scH}$), the charge is limited if the load is in generating mode. $r_2 > 0$ then has a linear relationship with $\tilde{v}_{sc}$. It also follows that the discharge is accelerated during a discharge operation.

- Otherwise ($v_{scl} \leq v_{sc} \leq v_{sch}$), r_2 is equal to zero, so that the controller operates as described in Section 4.2.

Fig. 3.b shows the value of r_2, which is always positive because $\mathcal{R}_d(x)$ is a positive semidefinite symmetric matrix. The value of r_2 is calculated so that $C_{sc}(CJ_{12}\,\tilde{v}_b + r_2 C_{sc}\,\tilde{v}_{sc}) = 0$, i.e., $i^*_{sc} = 0$ when $v_{sc} = v_{scL}$ or $v_{sc} = v_{scH}$. Implicitly, this does not allow v_{sc} to be lower than v_{scL} or greater than v_{scH}. It follows that:

- At $v_{sc} = v_{scL}$:

$$r_2 = -\frac{CJ_{12}\,\tilde{v}_b}{C_{sc}\,\tilde{v}_{sc}} = -\frac{CJ_{12}}{C_{sc}(v_{scL} - v^*_{sc})}\,\tilde{v}_b = -\sigma_L\,\tilde{v}_b \tag{25}$$

  with

$$\sigma_L = \frac{CJ_{12}}{C_{sc}(v_{scL} - v^*_{sc})},\ \sigma_L > 0 \tag{26}$$

- At $v_{sc} = v_{scH}$:

$$r_2 = -\frac{CJ_{12}\,\tilde{v}_b}{C_{sc}\,\tilde{v}_{sc}} = -\frac{CJ_{12}}{C_{sc}(v_{scH} - v^*_{sc})}\,\tilde{v}_b = \sigma_H\,\tilde{v}_b \tag{27}$$

  with

$$\sigma_H = -\frac{CJ_{12}}{C_{sc}(v_{scH} - v^*_{sc})},\ \sigma_H > 0 \tag{28}$$

The different values of r_2 can be summarized with several modes of operation as follows (see Fig. 4):

1. mode SCs 0: no limitation of SCs charge or discharge, i.e., $v_{scl} \leq v_{sc} \leq v_{sch}$, so $r_2 = 0$
2. if $v_{sc} < v_{scl}$:
   (a) mode SCs 1: if $\tilde{v}_b < 0$ then $r_2 = -\sigma_L \tilde{v}_b \frac{v_{scl} - v_{sc}}{v_{scl} - v_{scL}}$ in order to limit the discharge of the SCs gradually as a function of the SCs voltage.
   (b) mode SCs 2: if $\tilde{v}_b \geq 0$ then $r_2 = \sigma_L \tilde{v}_b \frac{v_{scl} - v_{sc}}{v_{scl} - v_{scL}}$ in order to increase the charge of the SCs compared to the previous control.
3. if $v_{sc} > v_{sch}$:
   (a) mode SCs 3: if $\tilde{v}_b < 0$ then $r_2 = -\sigma_H \tilde{v}_b \frac{v_{sch} - v_{sc}}{v_{sch} - v_{scH}}$ in order to increase the discharge of the SCs compared to the previous control, as well as to increase the convergence of v_b to v_b^*.
   (b) mode SCs 4: if $\tilde{v}_b \geq 0$ then $r_2 = \sigma_H \tilde{v}_b \frac{v_{sch} - v_{sc}}{v_{sch} - v_{scH}}$ in order to limit the charge of the SCs gradually as a function of the SCs voltage.

The major theoretical results of the controller are as follows:

- In order to counteract the non-injection of current in the DC bus by the SCs when the SCs voltage is lower than v_{scl}, the FC current is naturally increased based on (23) with the new term $r_2 \frac{v_{sc}}{v_{fc}} C_{sc}^2 \tilde{v}_{sc}$, which consequently preserves the stability of the whole closed-loop system.
- Therefore, during modes SCs 0 to 4, the dissipative resistance load does not need to be activated, which means $i_d^* = 0$.
- As mentioned in Section 4.2, r_1 is set to $\frac{v_{sc}\gamma}{v_b C^2}$, so that the FC does not control the DC bus voltage.
- The new term r_2 also integrates an implicit saturation function of the SCs current while preserving the stability of the whole closed-loop system. This property was not guaranteed with the controller in [31] and the *a posteriori* saturation function shown in Fig. 3.a.
- **An additional benefit of the new term r_2 is that it allows a boost charge or discharge of the SCs when the required operating conditions are satisfied.**

In summary, when there is no limitation (mode SCs 0), the control law is simplified with $r_2 = 0$ (see Section 4.2). For the situation of SCs voltage limitation (mode SCs = 1, 2, 3 or 4) the control

law is summarized as follows:

$$\begin{aligned}
\delta \dot{y} &= -y + i_l/v_b, \qquad \delta > 0 && (29)\\
i_{fc}^* &= \frac{v_b}{v_{fc}}\left(y v_b^* - \gamma \tilde{v}_{sc} - r_2 \frac{v_{sc}}{v_b} C_{sc}^2 \tilde{v}_{sc} \right), \qquad \gamma > 0 && (30)\\
i_{sc}^* &= -\gamma\, \tilde{v}_b + r_2 C_{sc}^2 \tilde{v}_{sc} && (31)\\
i_d^* &= 0 && (32)
\end{aligned}$$

4.4. SCs Current Limitations

If the SCs reference current exceeds the maximum allowed current ($-i_{sc_{max}}$), it will be limited at this value, which is called mode SCs 5. It follows that the dissipative load needs to be activated. The operation of the dissipative load is detailed in Section 4.6.

If the SCs current exceeds the maximum allowed current $i_{sc_{max}}$, it follows that the DC bus voltage falls. In such a case, the sizing of the system would need to be changed. However, it is possible to use the last term of (23) to take into account $\tilde{v}_b$ in the FC current equation. For that, r_1 is equal to $\mu \frac{v_{sc}\gamma}{v_b C^2}$, with $\mu > 1$, which leads to:

$$i_{fc}^* = \frac{v_b}{v_{fc}}\left(y v_b^* - \gamma \tilde{v}_{sc} - r_2 \frac{v_{sc}}{v_b} C_{sc}^2 \tilde{v}_{sc} + \frac{v_{sc}}{v_b}\gamma(1-\mu)\tilde{v}_b \right) \tag{33}$$

with $i_d^* = 0$, that is called mode SCs 6. This option is not recommended because it can possibly lead to fast variation of the FC current which in turn further degrades the FC remaining lifetime.

4.5. FC Current Limitations

If the FC reference current exceeds the maximum ($i_{fc_{max}}$), a flag mode FC is set to 7, where the FC current is limited at its maximum value. The mode FC 8 is used when the FC current is saturated at 0 ($i_{fc}^* = 0$). The dissipative load is activated according to (23), which is detailed in the next subsection.

4.6. Dissipative Load Operation

According to Sections 4.4 and 4.5, the dissipative load is activated when the current of the SCs or the FC is limited by its lower value (i.e., mode SCs = 5 or mode FC = 8). The dissipative load is expected to consume the extra energy. From (23), setting r_1 equal to $\mu \frac{v_{sc}\gamma}{v_b C^2}$, we have:

$$i_d^* = \frac{v_{fc}}{v_b} i_{fc}^* - y v_b^* + \gamma \tilde{v}_{sc} + r_2 \frac{v_{sc}}{v_b} C_{sc}^2 \tilde{v}_{sc} + \frac{v_{sc}}{v_b}\gamma(\mu - 1)\tilde{v}_b \tag{34}$$

The value of i_{fc}^* and μ depends on the mode of SCs and FC. Three different situations are detailed as follows:

1. mode SCs = 5 and mode FC $\neq$ 8:

   In this situation, since the FC power decreases slower than the load power, the SCs have to absorb power to stabilize the DC bus voltage. However, the SCs current is limited at its maximum value ($-i_{scmax}$) when it exceeds this value. Here, i_{fc}^* is represented by (30), which leads to:

   $$i_d^* = \frac{v_{sc}}{v_b}\gamma(\mu - 1)\tilde{v}_b \tag{35}$$

   Since the SCs are not capable of stabilizing the DC bus voltage in this case, the dissipative load has to take over the role of SCs. A good choice for μ is $1 + \frac{i_{sc}^{**} - i_{sc}^*}{\gamma \tilde{v}_b}$ where i_{sc}^{**} is the output of the saturation function of the SCs current, i.e., $i_{sc}^{**} = -i_{sc_{max}}$. We then have:

   $$i_d^* = \frac{v_{sc}}{v_b}(i_{sc}^{**} - i_{sc}^*) \tag{36}$$

   Reference current i_d^* represents the SCs current that could not be absorbed seen from the DC bus.

2. mode SCs $\neq$ 5 and mode FC = 8: In this situation, i_{fc}^* is set to 0, so only SCs, the dissipative load and the load in a generative mode are operating. Considering the energy efficiency, it seems natural to absorb all the load current by the SCs. Moreover, it is clear that if the dissipative load is set to zero, it is impossible to control the DC bus and SCs voltages at the same time. Therefore, in such case, two options appear:

   - $v_{sc} \leq v_{sch}$: Here r_2 is equal to zero and it can be shown that (31) leads to a steady state error in the DC bus voltage equal to $\tilde{v}_b = -\frac{v_b i_l}{\gamma v_{sc}}$.

     To counteract this issue, an integral term can be added without deteriorating the passivity properties [44] and leads to:

     $$i_{sc}^* = -\gamma \tilde{v}_b - x_c \quad \text{with} \quad \dot{x}_c = -k_i \tilde{v}_b \tag{37}$$

   - $v_{sc} > v_{sch}$: Although the SCs are still able to recharge from the DC bus, the extra energy from the load needs to be dissipated. In such circumtances, it is impossible to control at the same time the DC bus and SCs voltages. By setting $i_{fc}^* = 0$ in (30), we have:

     $$i_d^* = -y v_b^* + \gamma \tilde{v}_{sc} + r_2 \frac{v_{sc}}{v_b} C_{sc}^2 \tilde{v}_{sc} + \frac{v_{sc}}{v_b}\gamma(\mu - 1)\tilde{v}_b \tag{38}$$

Therefore, the term $\left(\gamma\tilde{v}_{sc} + \frac{v_{sc}}{v_b}\gamma(\mu-1)\tilde{v}_b\right)$ is set to zero, which leads to μ equal to $\left(1 - \frac{v_b\tilde{v}_{sc}}{v_{sc}\tilde{v}_b}\right)$. Then i_d^* is:

$$i_d^* = -yv_b^* + r_2\frac{v_{sc}}{v_b}C_{sc}^2\tilde{v}_{sc} \tag{39}$$

3. mode SCs = 5 and mode FC = 8: In this situation, both the SCs and FC currents are limited, i.e., $i_{sc}^{**} = -i_{sc_{max}}$, $i_{fc}^* = 0$, and $r_2 = 0$. Based on (34) and the previous method, we set μ equal to to $\left(1 + \frac{i_{sc}^{**} - i_{sc}^*}{\gamma\tilde{v}_b} - \frac{v_b\tilde{v}_{sc}}{v_{sc}\tilde{v}_b}\right)$, which leads to:

$$i_d^* = -yv_b^* + \frac{v_{sc}}{v_b}(i_{sc}^{**} - i_{sc}^*) \tag{40}$$

In summary, the effect of this dissipation strategy is to keep the DC bus voltage close to its reference level. While this impacts the energy efficiency, it guarantees the system stability, which is the main concern of short-term control.

Finally, all the detailed cases are summarized in Fig. 4.

5. Aging-Tolerant Control of PEMFC

As mentioned earlier, the FC performance tends to decrease over time, due to mechanical and electrochemical degradations. These phenomena reduce the FC's capacity for generating electric power (see Fig. 1). If the controller does not consider the aging of the FC, overload may happen and unstable behavior can be observed. For instance, when the FC SoH is 0.5, the FC maximum current is decreased by a factor of two (see Fig. 1). However, if this change inside the FC system is not considered, the top limit of the current saturation is still equal to 1500 A. If the load demand is high, then overload may occur and the control could diverge. Therefore, the estimation of the FC SoH should not be neglected and PHM of FCs is necessary. In this section, an aging-tolerant control of PEMFC is thus proposed, where the estimation of the SoH is realized by an EKF.

5.1. State-of-Health Estimation

An EKF is applied in this research to estimate the global SoH α_k and the speed of degradation β_k at instant k, as shown in Fig. 2. If the speed of degradation β_k is assumed constant between two successive discrete time steps, the SoH is linearly increasing, i.e., $\alpha(t) = \beta t + \alpha(0)$ and $\alpha[k] = \alpha[k-1] + \beta[k-1]T_s$. To handle changes in the speed of degradation, some slight random variations

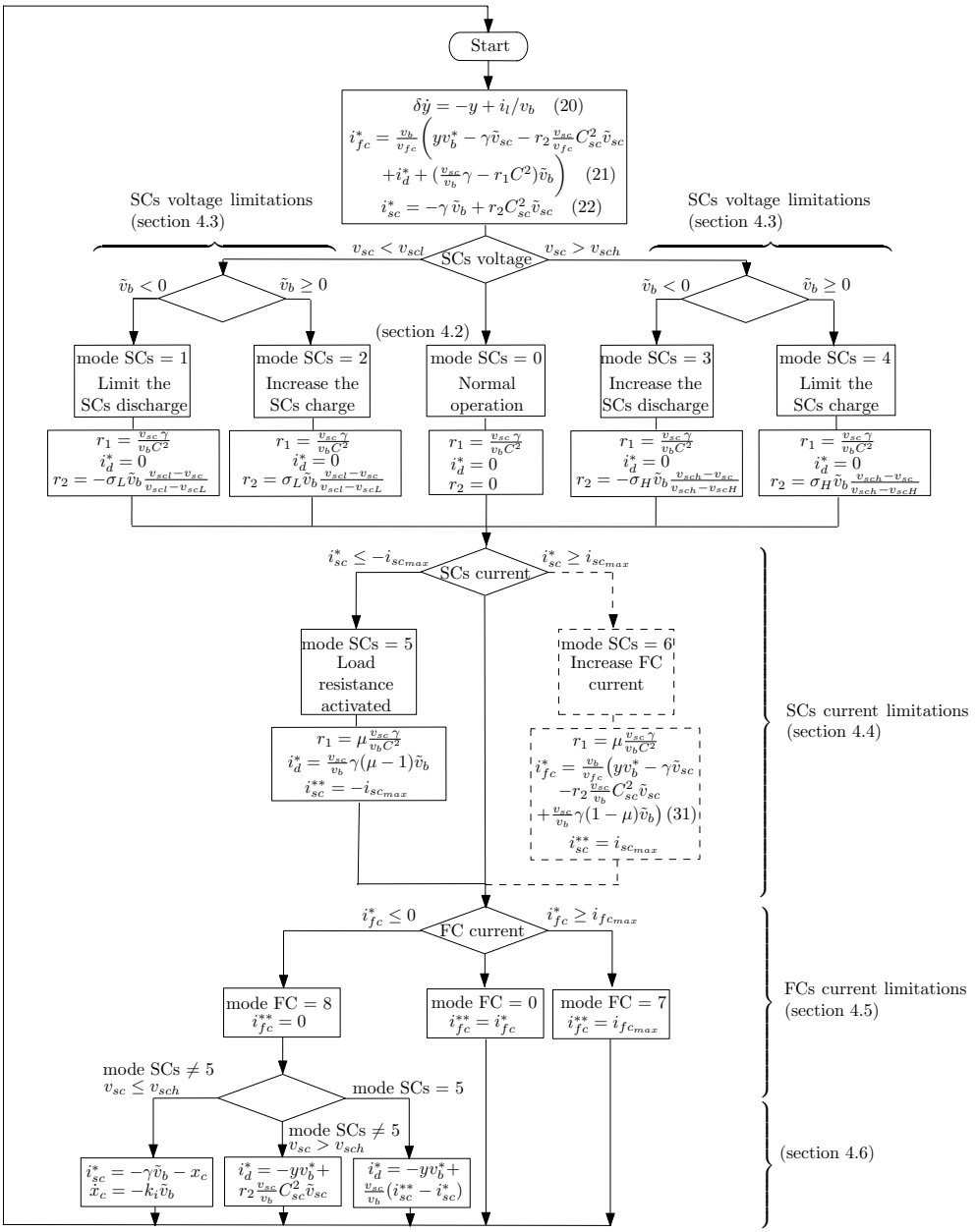

Figure 4: Flowchart of the proposed controller

of the speed of degradation must be allowed. This hypothesis leads to the two-dimensional discrete-time state space model [33, 34]:

$$x_{k|k-1} = Ax_{k-1|k-1} + \begin{bmatrix} 0 \\ 1 \end{bmatrix} w_{k-1} \tag{41}$$

with

$$A = \begin{bmatrix} 1 & T_s \\ 0 & 1 \end{bmatrix} \tag{42}$$

$$y_k = g(x_{k|k-1}, u_k) + v_k \tag{43}$$

where the state vector of the system is $x_k = [\alpha_k \ \beta_k]^T$, u_k represents the vector of the current and temperature inputs, y_k is the output voltage, T_s is the sampling period fixed at 1 s and w_k and v_k are the noise of process and observation assumed to be Gaussian with zero mean.

SoH α_k is set equal to zero at the beginning (i.e., no degradation), and increases to $\alpha_{max} = 0.3$ at the considered End of Life (EoL) of the FC [33, 34], representing a reduction of around 10% of the nominal power of the FC at 0.5 A/cm^2. At that time, the FC could continue to operate and the control can indicate that a maintenance is mandatory.

This threshold value α_{max} depends on the type of FC, and is either specified by the FC designer or by governmental rules. The US DOE target for 2020 is 5000 h of durability with cycling, with less than 10% of reduction of the nominal power at $1 - 1,5$ A/cm^2 [45]. Based on this considered value (10%) and the nominal current density, the value of α_{max} can be defined.

Since the voltage drop ΔV is not physically measurable and is caused by the concentration losses, activation losses and ohmic losses, the state vector is estimated from the stack voltage v_{fc}. Based on (1), $g(x_k, u_k)$ is expressed in discrete form as follows at time $t = kT_s$:

$$\begin{aligned} g(x_{k|k-1}, u_k) =& n\Big(E_0 - AT\ln\Big(\frac{j_k}{j_0}\Big) - R_0(1 + \alpha_{k|k-1})j_k \\ & - BT\ln\Big(1 - \frac{j_k}{j_{L0}(1 - \alpha_{k|k-1})}\Big)\Big) \end{aligned} \tag{44}$$

The EKF steps are then as follows:

- Initialization:

$x_{0|0} = E[x(t_0)], \quad P_{0|0} = Var[x(t_0)]$

- Prediction:

$x_{k|k-1} = Ax_{k-1|k-1}, \quad P_{k|k-1} = AP_{k-1|k-1}A^T + Q$

- Correction:

$K_k = P_{k|k-1}H_k^T(H_kP_{k|k-1}H_k^T + R)^{-1}$

with $\mathrm{H_k} = \frac{\partial \mathrm{g(x_k,u_k)}}{\partial \mathrm{x_k}}$

$P_{k|k} = P_{k|k-1} - K_k H_k P_{k|k-1}$

$x_{k|k} = x_{k|k-1} + K_k(V_{stk} - g(x_{k|k-1}, u_k))$

5.2. Maximum Power Point (MPP) of the FC

The FC SoH $\alpha_{k|k}$ and its derivative are estimated in real-time using (44). Then, the FC power can be expressed as a function of the load current so that the maximal power of the FC can be determined at each instant. Based on the simulation results using (44), it can be noted that the influence of the temperature is negligible. Therefore, the maximum current of the FC can be calculated by function $i_{fc_{max}}[k] = f(\alpha_{k|k})$, which describes the relationship between the SoH $\alpha_{k|k}$ and the maximum current. The function is fitted for an average FC temperature of 80°C as follows:

$$i_{fc_{max}}[k] = -1452.8\alpha_{k|k} + 1516 \tag{45}$$

The aging-tolerant control is realized based on the EKF associated with the MPP algorithm and a dynamic saturation function of the FC reference current, as shown in Fig. 2.

6. Algorithm validation and discussion

6.1. Simulation with a Modified NEDC Driving Cycle

The proposed system is tested via a simulation of the vehicle and the electrical components taken from [10] and [46]. Table 1 lists the parameter values used in the simulation.

The selected New European Driving Cycle (NEDC) is assumed to represent the typical usage of a car in Europe. Since the NEDC original cycle is not capable of meeting every case of limitation to test the correct operation of the proposed controller, a modified NEDC driving cycle is applied with the simulation. Here, the driving cycle includes four NEDC cycles during the first 80 s. One of these cycles is modified (between 40 s to 60 s) while the rest of the curve is unchanged, as shown in Fig. 5.a.

As the dynamics of power management and FC degradation are very different (degradation is typically observed over hundreds of hours), in this scenario, FC aging is artificially accelerated from 60 s to 100 s. The saturation of the FC current is updated dynamically based on the estimation

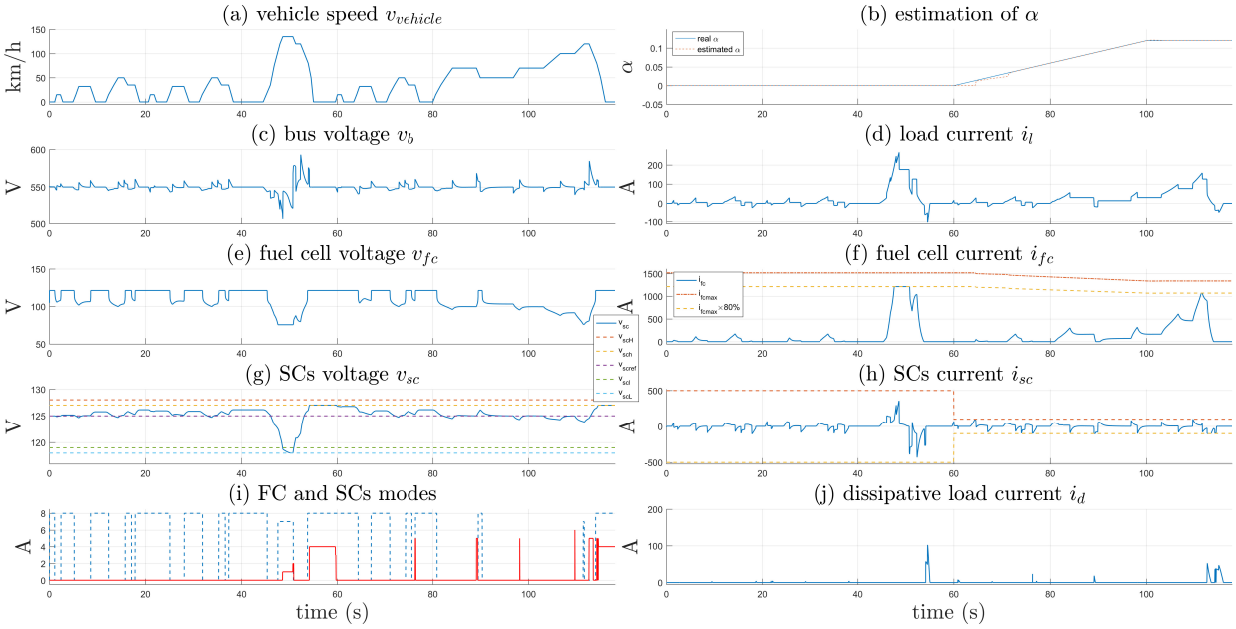

Figure 5: Simulation with a modified NEDC driving cycle

of the SoH shown in Fig. 5.b. We can notice that when the FC current is nil (or low in practical applications), the estimated parameters are not updated because the system is unobservable (60 s to 70 s). In order to protect the FC system, the saturation of the FC current is set to 80% of the MPP current (see Fig. 5.f).

Due to the term $(-\gamma\,\tilde{v}_b(t))$ in the control law of SCs reference current (see (24)) which represents the interconnections between elements, the FC supplies the energy at steady state while the SCs respond quickly during load power transients to stabilize the DC bus voltage (Fig. 5.c). The FC therefore has a smooth response, which increases its lifetime.

From 45 s to 50 s, the FC current is limited by the saturation function and the SCs supply the rest of the energy. This shows that when the power demanded by the load is greater than the maximum power of the FC, the FC power should be limited in order to protect the FC from overload and also ensure the whole controller stability. Without such algorithm, the system would not operate correctly.

The voltage of the SCs is limited between 119 V and 128 V, and v_{scl} and v_{sch} are fixed at 118 V and 127 V. The SCs current is limited to 500 A for the first 60 seconds and then to 50 A, respectively, for the purpose of the test. At 50s, due to parameter r_2 in the control law, modes 1

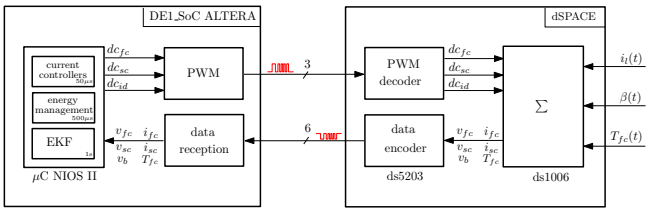

Figure 6: Hardware-in-the-loop scheme

and 2 are engaged when the SCs voltage is too low. This results in the limited drop in the DC bus voltage. After that, the vehicle speed decreases to zero, and it follows that the FC stops generating and SCs are charging from around 50 s to 55 s. Then, the SCs current goes to zero when the SCs voltage exceeds the limitation (mode 4) at around 55 s. There is also the limitation of SCs charging current (mode 5) at 75 s, 90 s and 98 s, as well as the limitation of the discharging current (mode 6) around 110 s. When the SCs charging current is limited (mode 5), or when the FC current is limited to zero (mode 8), the dissipating resistive load is activated to consume the extra energy and protect the system (see Fig. 5.j), according to (39).

6.2. Hardware-In-the-Loop Results

To further validate the real-time operation of the proposed passivity-based control and prognostic algorithm, an implementation and experiment was conducted using a HIL platform where the variation of the parameters of the FC model to emulate the aging is obtained from experimental data, as described in Section 2.1. The equipment under test is a control board based on a DE1_SoC INTEL/ALTERA FPGA board, where the algorithms are implemented in a NIOS II microcontroller.

Fig. 6 shows the structure of the HIL platform based on two equipments: 1) dSPACE boards to emulate the hybrid system and communicate with the controller, and 2) a DE1_SoC board for the implementation of the controller and EKF algorithms.

The DS1006 dSPACE board computes (1), (2), (3) and (4) every 50 μs via a Runge-Kutta algorithm. The designer can modify the load profile, FC temperature and speed of degradation ($\beta(t)$) of the FC. All the data necessary for the control and SoH estimation is sent to the ALTERA board with 32-bit serial ports (in 32Q14 format, i.e., 14 fractional bits) to emulate CAN converters. The data encoders are implemented in a VHDL black box from XSG (Xilinx System Generator). The 3 Pulse Width Modulation (PWM) signals generated by the ALTERA FPGA are decoded in

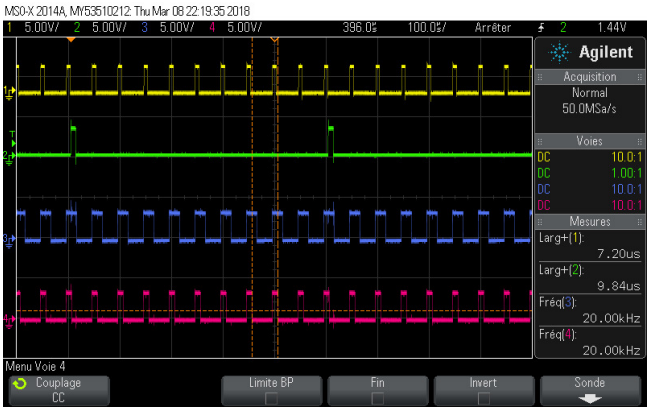

Figure 7: HIL scheme: 1) computation time of Timer 0, 2) computation time of Timer1, 3) FC PWM, 4) SCs PWM

the DS5203 dSPACE board to retrieve the duty cycle of the 3 converters.

The DE1_SoC ALTERA FPGA board is composed of 3 blocks: 3 PWMs, 6 data decoders and a NIOS II microcontroller. The algorithms are executed in 3 Interrupt Service Routines (ISR), based on 3 timers configured with a sampling time equal to 50 μs for the current loops and PWMs, 500 μs for the energy management, and 1 s for the EKF algorithm. Timer 0 for the current loop control uses a timeout pulse of one clock cycle in order to reset the PWM counter and therefore synchronize the ISR and PWM signals.

The 3 ISRs for the current loops, energy management, and EKF algorithm use vectorized interrupts. The computation times are respectively equal to 7.20 μs, 9.84 μs and 117 μs, as shown in Fig. 7.

The implementation of the proposed IDA-PBC does not introduce additional difficulty compared to regular controllers [31]. The only requirement is that the sampling time of the outer loop must be less than 5 ms [32]. That is the reason why a value equal to 500 μs is selected for energy management.

The sampling time of the EKF is fixed at 1 s for the purpose of the validation of all the algorithms in real-time. In a real context, a sampling time equal to 1 h seems sufficient in order to capture the evolution of FC degradation.

Fig. 8 shows the main data computed in the emulated system with the same scenario as in Fig. 5, where the aging speed of the FC is excessively increased for obvious practical reasons. Firstly, we can notice that the HIL results are similar to the ones in the Matlab/Simulink simulation. Secondly, we can observe in Fig. 8 that the FC current is well controlled by the NIOS II microcontroller and

does not exceed the maximum current fixed at 80% of the limit FC current. It means that the speed of degradation and the SoH of the emulated system are well estimated by the EKF algorithm computed in the NIOS II microcontroller, which guarantees that the maximum FC current follows (45).

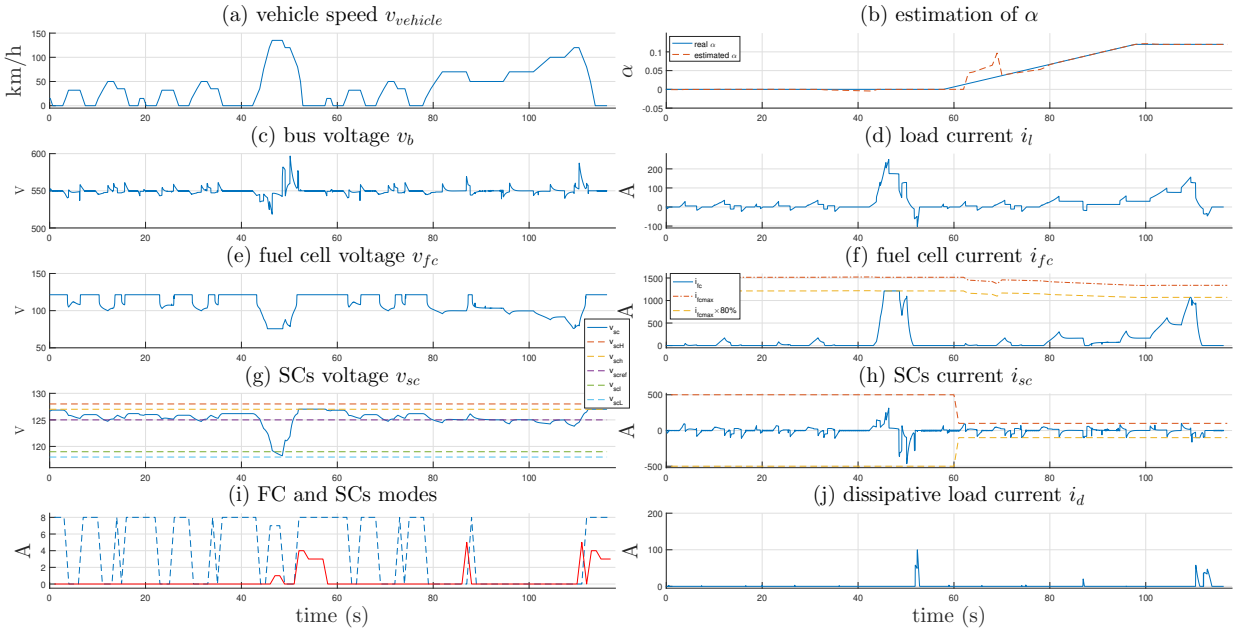

Figure 8: Hardware-in-the-loop platform results

6.3. Discussion

Firstly, Fig. 1 show that the FC power and maximum FC current are time dependent and that the aging of the FC is dependent on the industrial application. The lifespan of a PEMFC is still rather limited nowadays, with 2,500 hours on average under transportation operating conditions, which is inferior to the prerequisites from [45, 47]. As a consequence, PHM of FCs is mandatory for industrial applications.

PHM enables the planning of preventive maintenance at the right time, which can reduce costs due to irreversible damage. In other words, PHM can extend the life of such electrochemical converters using corrective actions, as proposed in this paper. This approach is therefore mandatory for the development of future FC vehicles.

Secondly, the decrease of FC maximum power over time directly impacts the power that the SCs need to provide, thereby reducing the closed-loop power management performance. It follows that

the design of the components needs to be made for long-term usage of the system. Consequently, the power management system needs to be evaluated with simulation and/or a hardware-in-the-loop platform during operating conditions where the FC is new and used before going to real experimental tests.

7. Conclusion

In this paper, an advanced controller was designed to manage power and energy between a hydrogen FC and SCs. The proposed passivity-based controller integrates some component constraints directly into the controller equations. In addition, an aging-tolerant control of the FC was also proposed and realized using an EKF. Simulation results showed that the controller proposed in this work ensures the integrity and an efficient exploitation of the components while preserving the locally asymptotic stability of the whole closed-loop system, and also protecting the system from overload. Finally, all the proposed algorithms were implemented in a soft-core NIOS II microcontroller in order to validate their operation in a real-time context before real experimentation tests.

Aknowledgement

This work was supported by the ANR DATAZERO project (contract ANR-15-CE25-0012), https://www.irit.fr/datazero/index.php/en/ and EIPHI Graduate School (contract ANR-17-EURE-0002).

[1] S. Yin, X. Li, H. Gao, O. Kaynak, Data-based techniques focused on modern industry: An overview, IEEE Transactions on Industrial Electronics 62 (1) (2015) 657–667.

[2] Z. Li, R. Outbib, S. Giurgea, D. Hissel, Diagnosis for pemfc systems: a data-driven approach with the capabilities of online adaptation and novel fault detection, IEEE Transactions on Industrial Electronics 62 (8) (2015) 5164–5174.

[3] S. Yin, S. X. Ding, X. Xie, H. Luo, A review on basic data-driven approaches for industrial process monitoring, IEEE Transactions on Industrial Electronics 61 (11) (2014) 6418–6428.

[4] K. Javed, R. Gouriveau, N. Zerhouni, P. Nectoux, Enabling health monitoring approach based on vibration data for accurate prognostics, IEEE Transactions on Industrial Electronics 62 (1) (2015) 647–656.

[5] M. Jouin, *all*, Estimating the end-of-life of pem fuel cells: Guidelines and metrics, Applied Energy 177 (2016) 87–97.

[6] M. Mohammedi, O. Kraa, M. Becherif, A. Aboubou, M. Ayad, M. Bahri, Fuzzy logic and passivity-based controller applied to electric vehicle using fuel cell and supercapacitors hybrid source, Energy Procedia 50 (2014) 619–626.

[7] P. Thounthong, P. Tricoli, B. Davat, Performance investigation of linear and nonlinear controls for a fuel cell/supercapacitor hybrid power plant, International Journal of Electrical Power & Energy Systems 54 (2014) 454–464.

[8] C. Sandoval, V. M. Alvarado, J.-C. Carmona, G. L. Lopez, J. Gomez-Aguilar, Energy management control strategy to improve the fc/sc dynamic behavior on hybrid electric vehicles: A frequency based distribution, International Journal of Renewable Energy 105 (2017) 407–418. doi:https://doi.org/10.1016/j.renene.2016.12.029.

[9] G. L. Lopez, R. S. Rodriguez, V. M. Alvarado, J. Gomez-Aguilar, J. E. Mota, C. Sandoval, Hybrid pemfc-supercapacitor system: Modeling and energy management in energetic macroscopic representation, International Journal of Applied Energy 205 (2017) 1478–1494. doi:https://doi.org/10.1016/j.apenergy.2017.08.063.

[10] O. Veneri, C. Capasso, S. Patalano, Experimental study on the performance of a zebra battery based propulsion system for urban commercial vehicles, Applied Energy 185 (2017) 2005–2018.

[11] A. M. Jarushi, N. Schofield, Battery and supercapacitor combination for a series hybrid electric vehicle, 5th IET International Conference on Power Electronics, Machines and Drives (PEMD) (2010).

[12] J. P. Torreglosa, P. Garcia, L. M. Fernandez, F. Jurado, Predictive control for the energy management of a fuel-cell–battery–supercapacitor tramway, IEEE Transactions on Industrial Informatics 10 (1) (2014) 276–285.

[13] R. T. Bambang, A. S. Rohman, C. J. Dronkers, R. Ortega, A. Sasongko, et al., Energy management of fuel cell/battery/supercapacitor hybrid power sources using model predictive control, IEEE Transactions on Industrial Informatics 10 (4) (2014) 1992–2002.

[14] I. Aharon, D. Shmilovitz, A. Kuperman, Multimode power processing interface for fuel cell range extender in battery powered vehicle, International Journal of Applied Energy 204 (2017) 572–581. doi:https://doi.org/10.1016/j.apenergy.2017.07.043.

[15] C. Capasso, O. Veneri, Integration between super-capacitors and zebra batteries as high performance hybrid storage system for electric vehicles, Energy Procedia 105 (2017) 2539–2544.

[16] X. Lu, X. Miao, W. Liu, J. Lu, Extension control strategy of a single converter for hybrid pemfc/battery power source, Internatinal Journal of Applied Thermal Engineering 128 (2018) 887–897.

[17] J. J. Moré, P. F. Puleston, C. Kunusch, M. A. Fantova, Development and implementation of a supervisor strategy and sliding mode control setup for fuel-cell-based hybrid generation systems, IEEE Transactions on Energy Conversion 30 (1) (2015) 218–225.

[18] N. Bizon, Optimal operation of fuel cell/wind turbine hybrid power system under turbulent wind and variable load, International Journal of Applied Energy 212 (2018) 196–209. doi:https://doi.org/10.1016/j.apenergy.2017.12.034.

[19] E. Eriksson, E. M. Gray, Optimization and integration of hybrid renewable energy hydrogen fuel cell energy systems - a critical review, International Journal of Applied Energy 202 (2017) 348–364.

[20] B. Amrouche, T. O. Cherif, M. Ghanes, K. Iffouzar, A passivity-based controller for coordination of converters in a fuel cell system used in hybrid electric vehicle propelled by two seven phase induction motor, International

Journal of Hydrogen Energy (2017).

[21] S. Mane, F. Kazi, N. Singh, Fuel cell and ultra-capacitor based hybrid energy control using ida-pbc methodology, in: Industrial Instrumentation and Control (ICIC), 2015 International Conference on, IEEE, 2015, pp. 879–884.

[22] F. Yang, B. Sheng, Y. Fu, Energy management for fuel cell-supercapacitor hybrid system using passivity-based controller with multi-equilibrium states, in: Industrial Electronics Society, IECON 2015-41st Annual Conference of the IEEE, IEEE, 2015, pp. 000511–000516.

[23] M. Phattanasak, W. Thammasiriroj, R. Gavagsaz-Ghoachani, M. Zandi, J. Martin, S. Pierfederici, B. Nahid-Mobarakeh, Hybrid power source fc/sc with single-loop control approach: Reference trajectories generation, IEEE Vehicle Power and Propulsion Conference (VPPC) (2017).

[24] S. Mane, M. Mejari, F. Kazi, N. Singh, Improving lifetime of fuel cell in hybrid energy management system by lure-lyapunov-based control formulation, IEEE Transactions on Industrial Electronics 64 (8) (2017).

[25] H. E. Fadil, F. Giri, J. Guerrero, A. Tahri, Modeling and nonlinear control of a fuel cell/supercapacitor hybrid energy storage system for electric vehicles, IEEE Transactions on Vehicular Technology 63 (7) (2014) 3011–3018.

[26] R. S. Ashok, Y. Shtessel, M. Ghanes, Sliding mode control of hydrogen fuel cell and ultracapacitor based electric power system: Electric vehicle application, IFAC Proceedings of 20th IFAC World Congress 50 (1) (2016) 14794–14799.

[27] J. Liu, Y. Zhao, B. Geng, B. Xiao, Adaptive second order sliding mode control of a fuel cell hybrid system for electric vehicle applications, Journal of Mathematical Problems in Engineering (2015).

[28] T. Allag, T. Das, Robust control of solid oxide fuel cell ultracapacitor hybrid system, IEEE Transactions on Control Systems Technology 20 (1) (2012).

[29] M. Wieczorek, M. Lewandowski, A mathematical representation of an energy management strategy for hybrid energy storage system in electric vehicle and real time optimization using a genetic algorithm, International Journal of Applied Energy 192 (2017) 222–233.

[30] C. Wu, J. Chen, C. Xu, Z. Liu, Real-time adaptive control of a fuel cell/battery hybrid power system with guaranteed stability, IEEE Transactions on Control Systems Technology 25 (4) (2017) 1394–1405.

[31] M. Hilairet, M. Ghanes, O. Bethoux, V. Tanasa, J. Barbot, D. Normand-Cyrot, A passivity-based controller for coordination of converters in a fuel cell system, Control engineering practice 21 (8) (2013) 1097–1109.

[32] M. Hilairet, O. Bethoux, M. Ghanes, V. Tanasa, J.-P. Barbot, M.-D. Normand-Cyrot, Experimental validation of a sampled-data passivity-based controller for coordination of converters in a fuel cell system, IEEE Transactions on Industrial Electronics 62 (8) (2015) 5187–5194.

[33] M. Bressel, M. Hilairet, D. Hissel, B. O. Bouamama, Extended kalman filter for prognostic of proton exchange membrane fuel cell, Applied Energy 164 (2016) 220–227.

[34] M. Bressel, M. Hilairet, D. Hissel, B. O. Bouamama, Remaining useful life prediction and uncertainty quantification of proton exchange membrane fuel cell under variable load, IEEE Transactions on Industrial Electronics 63 (4) (2016) 2569–2577.

[35] M. Bressel, M. Hilairet, D. Hissel, B. O. Bouamama, Fuel cell remaining useful life prediction and uncertainty quantification under an automotive profile, 42nd Annual Conference of the IEEE Industrial Electronics Society IECON 2016 (2016) 5477–5482.

[36] A. Isidori, Nonlinear control systems, Springer, 1995.

[37] S. A. Bhatti, S. A. Malik, A. Daraz, Comparison of p-i and i-p controller by using ziegler-nichols tuning method for speed control of dc motor, International Conference on Intelligent Systems Engineering (ICISE) (2016).

[38] M. Ehsani, Y. Gao, S. Longo, K. Ebrahimi, Modern electric, hybrid electric, and fuel cell vehicles, CRC press, 2018.

[39] D. Makarchuk, J. Kreicbergs, A. Grislis, M. Gailis, Analysis of energies and speed profiles of driving cycles for fuel consumption measurements, in: 14th International Scientific Conference Engineering for Rural Development, Latvia, 2015.

[40] R. Ortega, E. Garcia-Canseco, Interconnection and damping assignment passivity-based control: A survey, European Journal of Control 10 (2004) 432–450.

[41] J. LaSalle, Some extensions of lyapunov's second method, IRE Transactions on Circuit Theory 7 (1960) 520–527.

[42] A. Batlle, D. Cerezo, F. Colet, Robust hamiltonian passive control for higher relative degree outputs, ACES: Control Avancat de Sistemes d'Energia (2006).

[43] T. Azib, O. Bethoux, C. Marchand, E. Berthelot, Supercapacitors for power assistance in hybrid power source with fuel cell, in: Industrial Electronics, 2009. IECON'09. 35th Annual Conference of IEEE, IEEE, 2009, pp. 3747–3752.

[44] A. Donaire, S. Junco, On the addition of integral action to port-controlled hamiltonian systems, Automatica 45 (8) (2009) 1910–1916.

[45] U.S. department of energy (doe) technical targets for polymer electrolyte membrane fuel cell components, Tech. rep. (2018).

[46] O. Veneri, C. Capasso, S. Patalano, Experimental investigation into the effectiveness of a super-capacitor based hybrid energy storage system for urban commercial vehicles, Applied Energy 227 (2018) 312–323.

[47] W. Schmittinger, A. Vahidi, A review of the main parameters influencing long-term performance and durability of pem fuel cells, International Journal of Power Sources 180 (1) (2008) 1–14.

Fuel cell parameters	
FC current i_{fc}	[A]
FC voltage v_{fc}	[V]
FC current density j_{fc}	[A/cm^2]
FC temperature T_{fc}	[K]
Number of cells n	53
Maximum FC voltage E_0	57.50
Activation surface S	220 cm^2
Global resistance R	0.001 [Ω]
Activation constant A	0.6×10^{-4}
Concentration constant B	-1.5×10^{-4}
Exchange current density j_0	9.4174×10^{-4} [A/cm^2]
Limiting current density j_L	1 [A/cm^2]
Number of FC packs in series N_{fcs}	2
Number of FC packs in parallel N_{fcp}	8
Vehicle parameters	
Vehicle velocity $V_{vehicle}$	[m/s]
Transmission efficiency $\eta_{traction}$	0.95
Vehicle weight (without passengers) $M_{vehicle}$	1820 [kg]
Front surface $S_{vehicle}$	3.664 [m^2]
Gravitational acceleration g	9.8 [m/s]
Aerodynamic drag coefficient C_x	3.664
Air density ρ	1.225 [kg/m^3]
Hybrid system parameters	
DC bus voltage v_b	[V]
SCs voltage v_{sc}	[V]
SCs current i_{sc}	[A]
Load current i_l	[A]
Controllable load current i_d^*	[A]
DC bus capacity C	9×10^{-3} [F]
SCs capacity C_{sc}	63 [F]
FC inductance L_{fc}	200 [mH]
SCs inductance L_{sc}	200 [mH]
Controller parameters	
γ	10
δ	2
IP controller proportional gain	0.384
IP controller integral gain	184.32
Current sampling time	50 [μs]
Voltage sampling time	500 [μs]
EKF parameters	
State of health $\alpha(t)$	
Speed of degradation $\beta(t)$	
EKF sampling time T_s	1 [s]
$\mathcal{R}$	10^{-3}
Covariance matrix $\mathcal{Q}$	diag(0, 3×10^{-6})
Initial matrix $P[0\|0]$	diag(0, 0)

Table 1: Nomenclature and system parameters.